nature communications

Article

https://doi.org/10.1038/s41467-025-57942-z

Interplay between hole superconductivity and quantum critical antiferromagnetic fluctuations in electron-doped cuprates

Received: 7 September 2023

Accepted: 3 March 2025

Published online: 20 March 2025

Check for updates

Dongjoon Song[1,2,13], Suheon Lee[3,4,13], Zecheng Shen[5], Woobin Jung[2,6], Wonjun Lee[7], Sungkyun Choi[3,4], Wonshik Kyung[2,6], Saegyeol Jung[2,6], Cheng-Maw Cheng[8], Junyoung Kwon[9], S. Ishida[10], Y. Yoshida[10], Seung Ryong Park[11], H. Eisaki[10], Yao Wang[5] ✉, Kwang-Yong Choi[12] ✉ & C. Kim[2,6] ✉

Antiferromagnetic spin fluctuations are the most promising candidate as the pairing glue of high critical temperature (T_c) superconductivity in cuprates. However, many-body states and intertwined orders have made it difficult to determine how electrons couple with fluctuating spins to form Cooper pairs. Recent experimental and theoretical studies have suggested spin fluctuation-driven quasiparticle band folding, but the relationship between the resultant Fermi pockets and superconductivity remains unclear. Here, using angle-resolved photoemission spectroscopy and numerical simulations, we show a proportional relationship between T_c and the quasiparticle weight of the incipient hole pocket near the nodal point in electron-doped $Pr_{1-x}LaCe_xCuO_{4\pm\delta}$. Through complementary muon spin spectroscopy measurements, we uncover that the hole pocket forms only in the regime of the fluctuating antiferromagnetic ground state around a presumed quantum critical point. Our observations highlight the significance of the electron-spin fluctuation interaction in enhancing the hole pocket and consequently driving superconductivity.

The microscopic mechanism of high critical temperature (T_c) superconductivity in cuprates has been a mystery for the last four decades. While various exotic phases, such as pseudogap, charge order, and strange metal phases, have been found in over 200 compounds, one of the most fundamental features in doping–temperature (T) phase diagrams of cuprates is that T_c forms a dome-like region near the antiferromagnetic (AF) order phase boundary[1–3]. This proximity of superconductivity and AF order makes AF spin fluctuation a compelling candidate as the pairing glue that mediates superconductivity. Theoretical studies in support of this conjecture have well elucidated the unconventional d-wave pairing symmetry observed in curates using electron-AF spin fluctuation coupling[4,5]. On the experimental side, quasiparticles and their renormalization attributed to many-body interactions have been directly observed by angle-resolved

[1]Stewart Blusson Quantum Matter Institute, University of British Columbia, Vancouver, BC V6T 1Z4, Canada. [2]Center for Correlated Electron Systems, Institute for Basic Science (IBS), Seoul 08826, Korea. [3]Center for Integrated Nanostructure Physics, Institute for Basic Science (IBS), Suwon 16419, Korea. [4]Sungkyunkwan University, Suwon 16419, Korea. [5]Department of Chemistry, Emory University, Atlanta, GA 30322, USA. [6]Department of Physics and Astronomy, Seoul National University, Seoul 08826, Korea. [7]Rare Isotope Science Project, Institute for Basic Science (IBS), Daejeon 34000, Korea. [8]National Synchrotron Radiation Research Center, Hsinchu City 300092, Taiwan. [9]Department of Physics, Pohang University of Science and Technology, Pohang 37673, Korea. [10]National Institute of Advanced Industrial Science and Technology (AIST), Tsukuba, Ibaraki 305-8568, Japan. [11]Department of Physics, Incheon National University, Incheon 22012, Korea. [12]Department of Physics, Sungkyunkwan University, Suwon 16419, Korea. [13]These authors contributed equally: Dongjoon Song, Suheon Lee. ✉e-mail: yao.wang@emory.edu; choisky99@skku.edu; changyoung@snu.ac.kr

photoemission spectroscopy (ARPES)[6,7]. Although substantial progress has been made in understanding the electron-boson scattering, demonstrating how the spin fluctuation coupling specifically dresses the electrons and manipulates the superconductivity remains a spectroscopic challenge because the complex phase diagram and strong electron correlation complicate the interpretation of quasiparticle spectra.

For the interaction of electrons with the AF order, one of the most widely accepted features demonstrated by early ARPES and concomitant mean-field studies is that the emergence of a long-range (LR)-AF super-lattice potential with under-electron doping results in the folding of the quasiparticle band and reconstructs the Fermi surface from a large circle (*L*-circle) to small hole (*h*-) and electron (*e*-) pockets (Fig. 1 and Supplementary Fig. 1)[6–9]. In addition to this mean-field scheme with the LR order, further low-energy spectral analysis also found traces of the reconstructed Fermi pockets in the doping range of the superconducting (SC) phase beyond the LR-AF order phase boundary[10–12], pointing to the possible contributions from the short-range (SR)-AF fluctuations or topological orders[10]. Moreover, it has been even argued that both folded AF and unfolded pristine components are detected simultaneously in the single-particle ARPES spectrum[7,13], which is subject to the strong electron correlation. To date, a complete understanding of the exotic folding behavior is still lacking, calling for more sophisticated spectral analysis.

Although the folding effect is still difficult to define in the SC region, experimental evidence indicating the possible correlation between the superconductivity and one of the AF pockets has been reported through magneto-transport studies. Previous magnetoresistance and Shubnikov–de Haas quantum oscillation measurements on electron-doped $Nd_{2-x}Ce_xCuO_{4\pm\delta}$ observed clues of the *h*-pocket contribution to the conductivity only in the doping range of the SC region[11,12], suggesting that spin-coupled quasiparticles on the *h*-pocket play a crucial role in driving the superconductivity. However, it is still debated whether the external magnetic field applied for those magneto-transport measurements not only suppresses the superconductivity but also reinforces the AF order and pins the pockets to the system. Therefore, at least two important, related questions remain to be answered regarding the *h*-pocket-driven superconductivity: is the *h*-pocket tied to the superconductivity even in ambient conditions without an external magnetic field? and if this is the case, which magnetic ground state gets along with the pocket state?

To resolve this puzzle, we carried out ARPES and zero-field muon spin rotation/relaxation (μSR) measurements on the electron-doped cuprate $Pr_{1-x}LaCe_xCuO_{4\pm\delta}$ (PLCCO), followed by spectral simulations with the Hubbard model. By scrutinizing the low-energy photoemission spectra near the Fermi energy (E_F), we found that the single-particle spectrum of the nodal quasiparticle band of PLCCO consists of both folded AF and unfolded pristine components, as also shown by our numerical calculations based on cluster perturbation theory (CPT). Tracking the doping evolution of the folded AF branch, we reveal that the superconductivity develops as the folded hole band component incipiently crosses the E_F in the SR-AF ground state region around a putative quantum critical point (QCP) where the static-to-dynamic AF quantum phase transition occurs. Furthermore, we find that the zero-energy quasiparticle weight of the hole band Z_{hole} is in proportion to T_c, while the gap from the band top to E_F is negatively correlated with T_c. These results suggest that the incipient hole band that forms the underlying *h*-pocket is driven by

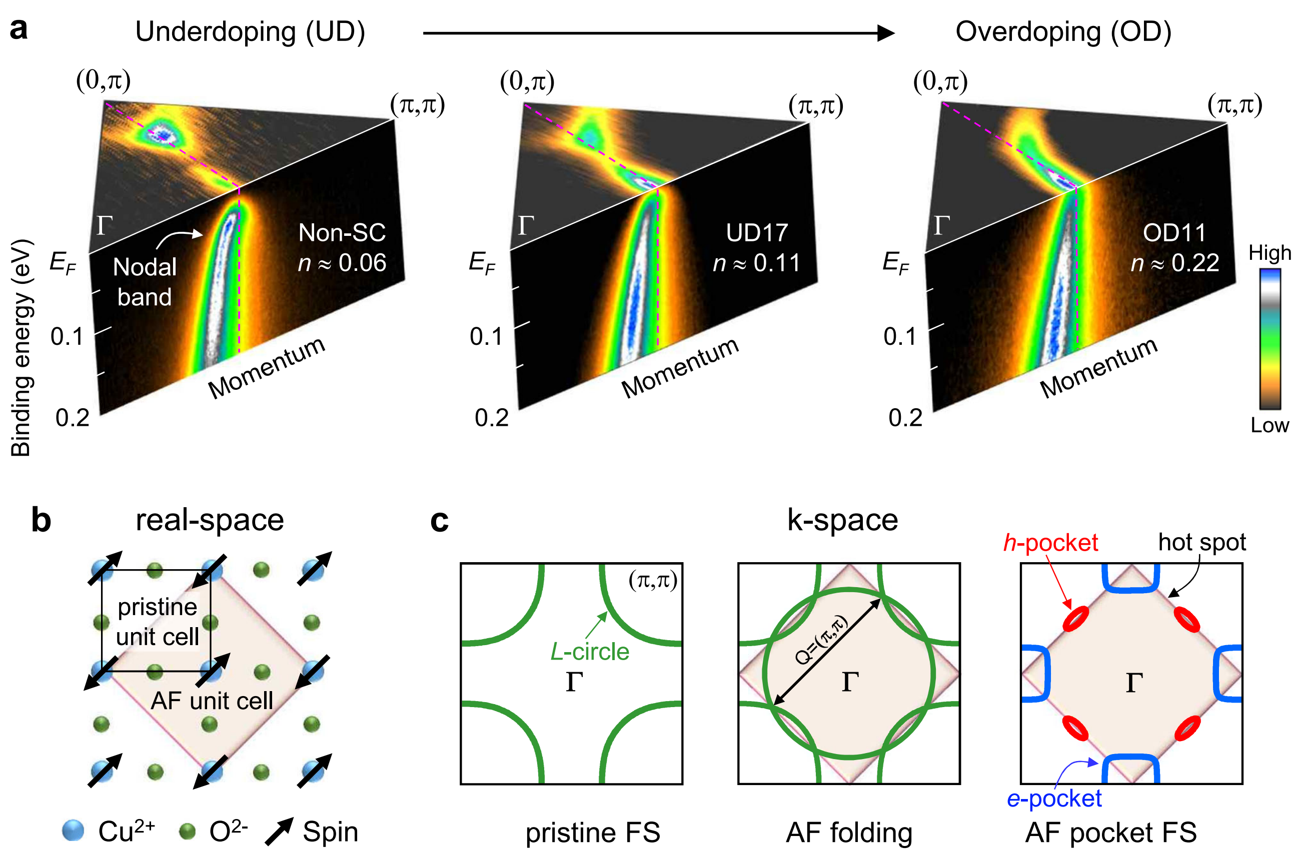

Fig. 1 | Electronic structure and antiferromagnetic (AF) band reconstruction of electron-doped cuprates. a Fermi surface (FS) and nodal band ARPES spectra of PLCCO as a function of electron doping (n). Non-SC, UD17, and OD11 indicate non-superconducting, underdoping, and overdoping, respectively, where the number indicates T_c in Kelvins. **b** Copper oxide plane with antiferromagnetically ordered spins. The black lines show the pristine unit cell, and the pink-shaded square is the AF unit cell. **c** Schematics of pristine (left) and AF pocket (right) FSs of electron-doped cuprates. The middle panel shows the band-folding process, attributed to the AF unit cell doubling shown in **b**. The pink-shaded area is the AF Brillouin zone.

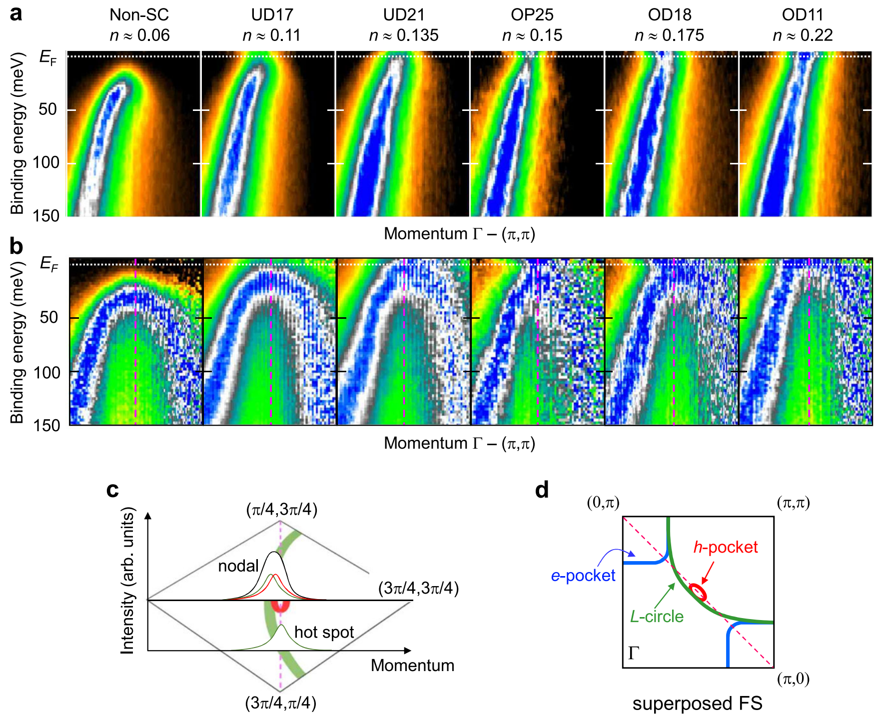

Fig. 2 | Doping evolution of the nodal band in PLCCO. **a** ARPES spectra of the nodal band after Fermi–Dirac correction for various doping samples. OP indicates optimal doping. **b** Nodal band spectra with the maximum energy distribution curve (EDC) that brightens the "folded shadow band" forbidden in (**a**) (see Supplementary Fig. 3). **c** Schematic spectra of the FS at the nodal point and hot spot. The black peak at the nodal point indicates the nodal band spectrum. The red and green peaks show the hole (h-) pocket and large (L-) circle components, respectively. **d** Superposed FS consisting of electron (e-) pocket, h-pocket, and L-circle. The pink dashed lines mark the AF zone boundary.

electron-spin fluctuation interaction and plays a crucial role in the emergence of superconductivity.

Results

Correlation between superconductivity and hole pocket

Figure 2a shows the doping-dependent ARPES spectra of the low-energy quasiparticle state dispersing along the nodal direction, the so-called "nodal band", after dividing the Fermi–Dirac distribution (also see Supplementary Fig. 2a). The most under-doped (UD) sample with $n \approx 0.06$, referred to as Non-SC, exhibits a clear energy gap that seems to close gradually as the electron doping n increases. According to the mean-filed picture, the gap originates from the splitting of the quasi-particle band into upper and lower bands due to effective $\mathbf{Q} = (\pi, \pi)$ AF scattering, and the gap closing signals a dissipation of AF super-lattice potential (Fig. 1 and Supplementary Fig. 1)[7–9]. Although the AF band reconstruction is expected to result in the band folding, the folded AF branch is invisible in the raw spectra (Fig. 2a) because its intensity is weak due to the matrix-element effect[6]. The shadow AF branch indeed comes into view with a two-dimensional stacking of energy distribution curves (EDCs) when the folding effect is strong enough. For example, in the EDC plots of the nodal band spectra in Supplementary Fig. 3, the flattened band top and the back bending of the band are well-defined for the heavily under-doped samples ($n \approx 0.06$ and 0.11). In addition, we get even better visibility of the shadow branch by normalizing the maximum intensity of the EDCs at each momentum, as displayed in Fig. 2b (for details of the analysis, see Supplementary Fig. 4)[14]. Accordingly, the total hole band dispersion with the folding center at the AF zone boundary (pink dashed line) is obviously seen in the normalized spectra of those under-doped samples ($n \approx 0.06$ and 0.11 in Fig. 2b).

On the other hand, the spectrum of the AF branch becomes scattered and less well-defined with optimal and overdoping even in the analyzed spectra (to the right of the pink dashed line for $n \approx 0.135$ and above in Fig. 2b). At the same time, the spectrum around the folding center is significantly broadened, and the band top is no longer immediately discernible due not only to the weakening of folding effect but also to the strong enhancement of in-gap spectral intensity (see the schematic nodal spectrum in Fig. 2c). In the electron-doped cuprates, the enhancement of the in-gap spectral weight has been considered to result from the growth of the unfolded pristine state[15–17]. As such, the simultaneous observation of the AF branch and the in-gap spectrum signals that PLCCO virtually has a superposed Fermi surface consisting of the AF pockets and the pristine L-circle components[13] (Fig. 2d). From the theoretical perspective, such a superposition is beyond the conventional mean-field picture but is associated with the many-body effect in the fluctuating correlated electron system[11,13,18–20]. From a phenomenological standpoint, it represents the coexistence of spin-interacting and spin-non-interacting states in a single-particle spectral function. Considering that the spin-interacting electrons form the h-pockets, extracting the AF components from the nodal band spectra would be a starting point for understanding the relationship between the h-pocket and superconductivity. However, it is a technically challenging issue.

To address this challenge, we attempted a phenomenological analysis based on the variation in the spectral distributions along the Fermi surface. Specifically, we paid attention to the spectrum measured at the position of the hot spot as it also undergoes a similar in-gap state filling to the nodal band spectrum but has the folding band at much deeper binding energy (Supplementary Fig. 2)[15–17]. Figure 3a displays the doping-dependent EDCs obtained by integrating the spectrum within a small momentum window around the folding center of the nodal and hot spot band spectra, marked as "nodal" and "hot spot". For the Non-SC sample with $n \approx 0.06$, both the nodal and hot spot EDCs show clear AF gaps with peak energy ~30 and ~100 meV,

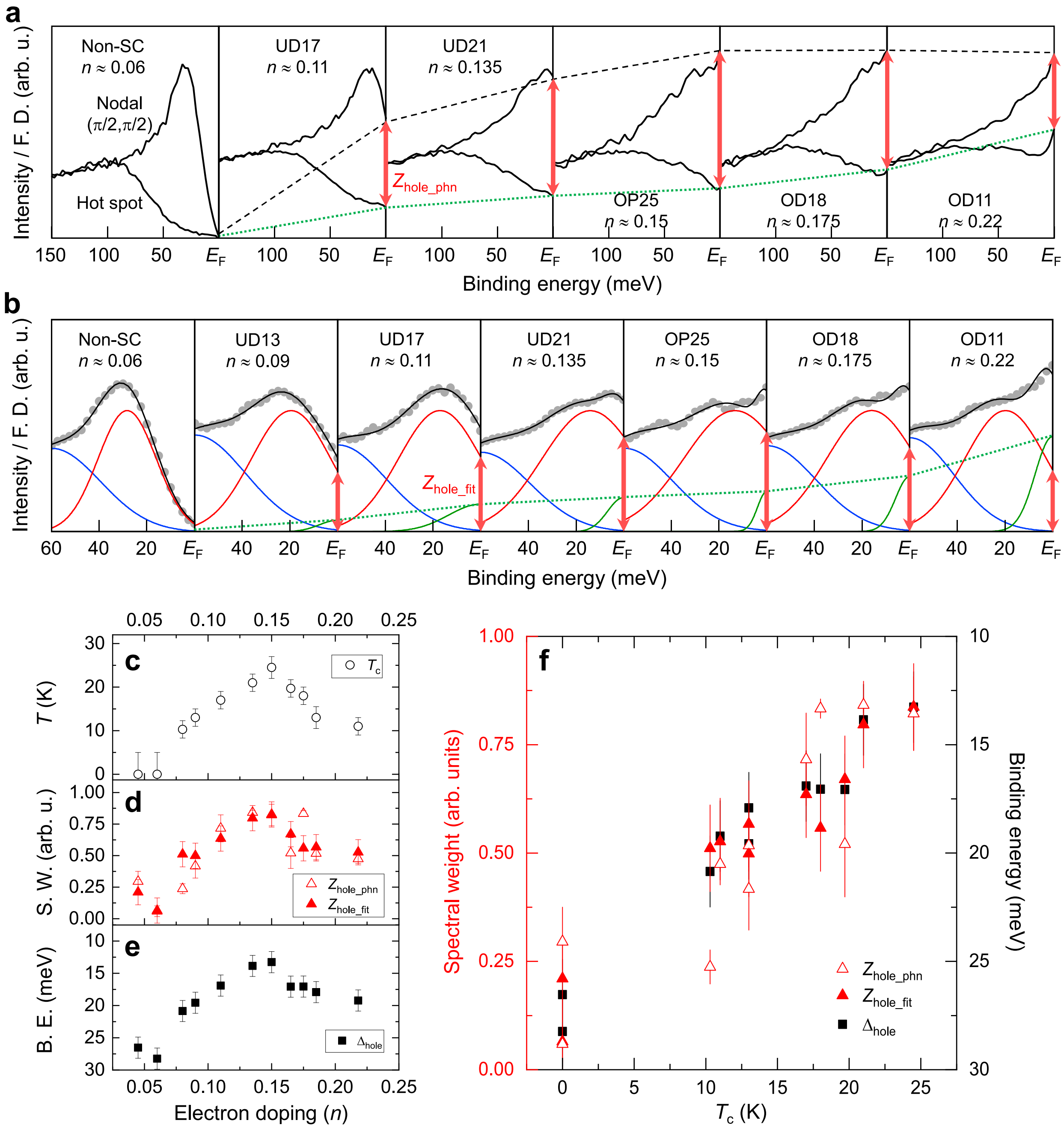

Fig. 3 | Correlation between the Fermi hole pocket and superconductivity. **a** EDCs at (π/2, π/2) and hot-spot point for various dopings. Black dashed and green dotted lines guide the eye to the zero-energy intensity of each EDC. **b** EDCs at (π/2, π/2) with Gaussian function fitting results. Red, green, and blue solid lines correspond to AF peak, in-gap pristine peak, and background, respectively. The red vertical arrows in **a**, **b** denote Z_{hole} obtained by the phenomenological method (Z_{hole_phn}) and the Gaussian fitting (Z_{hole_fit}). **c**, **d**, **e** T_c, Z_{hole_phn}, Z_{hole_fit}, and Δ_{hole} as a function of n, where Δ_{hole} is a binding energy of AF peak obtained by the Gaussian fitting. **f** Z_{hole_phn}, Z_{hole_fit}, and Δ_{hole} as a function of T_c. Error bars of Z_{hole_phn} represent signal-to-noise error. Error bars of Z_{hole_fit} and Δ_{hole} are determined based on the fitting error of the EDC peak.

respectively, with almost negligible in-gap spectral intensity at E_F. With increasing doping, the zero-energy intensity dramatically enhances at both points (see doping evolution of black dashed and green dotted lines in Fig. 3a). Because of its subtle gap, a strong intermixing of the folded and unfolded components is expected in the in-gap zero-energy states of the nodal EDC. (see the nodal spectra of the SC samples in Fig. 2c). On the other hand, due to a relatively large gap size, the in-gap zero-energy state at the hot spot is considered to be dominated by the pristine component with a tiny fraction of the AF component (see the hot-spot spectrum in Fig. 2c)[16]. In this framework, assuming that the pristine Fermi surface has a nearly momentum-invariant spectral weight distribution along the L-circle contour[7–9,21], the difference in the zero-energy spectral intensity between the nodal and hot spot approximately provides the quasiparticle weight of the folded band Z_{hole_phn} that contributes to the formation of the underlying h-pocket (see red arrows in Fig. 3a).

Based on this phenomenological perspective, we obtained Z_{hole_phn} from all measured samples and plotted it in Fig. 3d as a

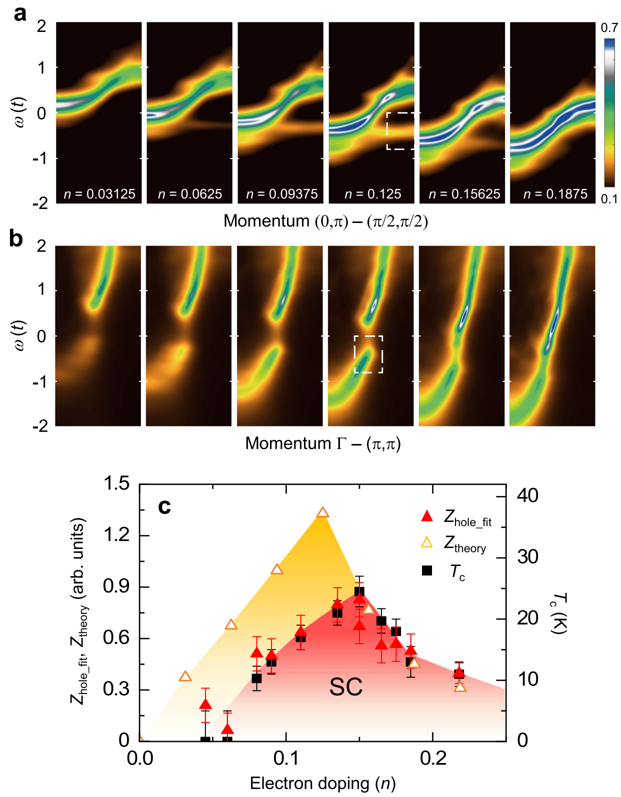

Fig. 4 | Numerically calculated electronic structures of PLCCO based on cluster perturbation theory (CPT). a, b Simulated $A(\mathbf{k}, \omega)$ at high symmetry cut: (0, π) to (π/2, π/2) and Γ to (π, π), respectively. The white dashed boxes highlight the nodal hole band top, where the spectral weight is integrated to get Z_{theory}. **c** Z_{hole}, Z_{theory}, and T_c, as a function of n. Error bars of Z_{hole_fit} are determined based on the fitting error of the EDC peak shown in Fig. 3.

function of n. At a glance, it shows dramatic doping evolution with the maximum around the optimal doping, contradicting the monotonic increase of the in-gap pristine spectral weight (green dotted line in Fig. 3a). Interestingly, Z_{hole_phn} exhibits a dome-shaped doping dependence, which resembles the T_c evolution (Fig. 3c, d). This similar doping dependence between Z_{hole_phn} and T_c is shown as a proportional relationship in Fig. 3f; Z_{hole_phn} linearly increases with increasing T_c. This result provides a couple of valuable insights into the SC nature associated with the h-pocket. Firstly, given that the Z_{hole_phn} measures the occupancy of the hole band state at E_F, the correlation between Z_{hole_phn} and T_c suggests that the density of state (DOS) of the h-pocket is a key determinant of T_c. Simultaneously, it also highlights that the pair interaction between the holes at the pockets plays a crucial role in mediating the superconductivity. From this aspect, the holes are viewed as quasiparticles dressed by AF fluctuations, which have been theoretically known to induce pairing correlations in both the perturbative[22] and strongly correlated regime[23]. These interpretations are supported by our numerical calculations as well as μSR analysis, shown in the following sections.

In addition to the phenomenological analysis, we carried out a function-fit analysis on the nodal band spectra without involving the hot-spot spectra. The nodal EDCs could be well fitted with three Gaussians: AF peak, in-gap pristine peak, and high-binding energy background (see the red, green, and blue lines, respectively, in Fig. 3b), where the AF peak represents the leading peak of the hole band and its spectral weight at E_F corresponds to the h-pocket quasiparticle weight (see Z_{hole_fit} with red arrows in Fig. 3b). The resulting quasiparticle weights Z_{hole_phn} and Z_{hole_fit}, obtained by the phenomenological method and the Gaussian fitting, respectively, show quite similar doping-dependent behaviors. Furthermore, we carried out a Lucy-Richardson deconvolution[24] to rule out the experimental resolution effect (see Supplementary Note 2). In consequence, we obtained a consistent result from the deconvoluted data (Supplementary Fig. 5). This additional analysis confirms that the proportionality between Z_{hole} and T_c is a robust result regardless of the analysis method employed. Meanwhile, electron-phonon coupling also causes renormalization of the electronic structure. However, its effect on the zero-energy quasiparticle weight was found to be insignificant.

We highlight that the function fitting also allows us to determine the AF peak position Δ_{hole} even in the overdoping region where the peak shape is ambiguous due to strong in-gap pristine intensity. We define the energy gap Δ_{hole} as the binding energy of the hole band top. Figure 3e displays Δ_{hole} with an inverted axis as a function of n. Intriguingly, Δ_{hole} shows a doping evolution similar to Z_{hole} and T_c (Fig. 3c–e), suggesting a negative correlation between Δ_{hole} and T_c (see Fig. 3f); T_c increases with decreasing Δ_{hole}. It is noteworthy that the hole band retains a shallow gap Δ_{hole} = ~13 meV even at the optimal doping $n \approx 0.15$ (Fig. 3e), indicative of the gap over the entire SC region. A recent high-resolution ARPES study also observed a similar AF gap in the nodal band of optimally electron-doped $Nd_{2-x}Ce_xCuO_{4\pm\delta}$ ($x = 0.15$)[13]. On the other hand, Δ_{hole} larger than 26 meV completely rules out the superconductivity (see the linear fitting result in the Supplementary Note 2 and Supplementary Fig. 6). The shallow ($\Delta_{hole} < 26$ meV) and large gap ($\Delta_{hole} > 26$ meV) in the SC and non-SC samples are reminiscent of incipient band pairing and its pairing cut-off energy, respectively[25].

Numerical simulations of the hole pocket

We argue that the unconventional reconstruction of the Fermi surface, characterized by the coexisting L-circle and pockets, originates from strong correlations instead of static disorder. To demonstrate this, we simulated the single-band Hubbard model, a many-body model that describes the physics of cuprates, using CPT[26,27]. The CPT spectral simulation, invoking both electron correlations and SR-AF fluctuations, allows us to trace the evolution of the AF branch. Figure 4a, b show the resulting electronic structure as a function of n (see Methods and Supplementary Fig. 7 for details of the simulation). Unlike the single-band folding predicted by mean-field theory, the simulated spectral functions of this strongly correlated system show the coexistence of two peaks near the nodal Fermi surface. Although the two peaks are sharper and more separated in the simulation obtained from the clean model, the overall trend is consistent with the experimental findings that show an increase in the in-gap spectral weight at the hot spot, resulting in a peak-dip-hump-like feature in the EDC of OD samples (see Fig. 3a)[16,17].

By integrating the simulated single-particle spectrum around the folding center (π/2, π/2) of the hole band (inside the white dashed boxes in Fig. 4a, b), we further estimate the theoretical quasiparticle weight Z_{theory}. Figure 4c presents Z_{theory}, along with Z_{hole_fit} and T_c, as a function of n. The overlap of Z_{hole_fit} and the SC domes again shows the scaling relation between Z_{hole} and T_c. The concurrent dome-shaped doping dependence of Z_{theory} further indicates the role of the marked interplay of the electron correlation and AF fluctuations in shaping the observed Z_{hole} dome. If the AF fluctuations act as the pairing glue[21], the dome structure of Z_{hole}, and consequently T_c, can be interpreted as the result of gradually developed quasiparticles with AF fluctuations. The quantitative difference between Z_{hole} and Z_{theory} is mainly due to two factors. First, the simplicity of the single-band Hubbard model and finite-size simulation neglects the impact of orbital fluctuations and LR interactions, which affect the self-energy. Second, while Z_{hole} is obtained by integrating the experimental spectral weight in the immediate vicinity of E_F, a comprehensive description of quasiparticles should involve a wider energy window.

 https://doi.org/10.1038/s41467-025-57942-z

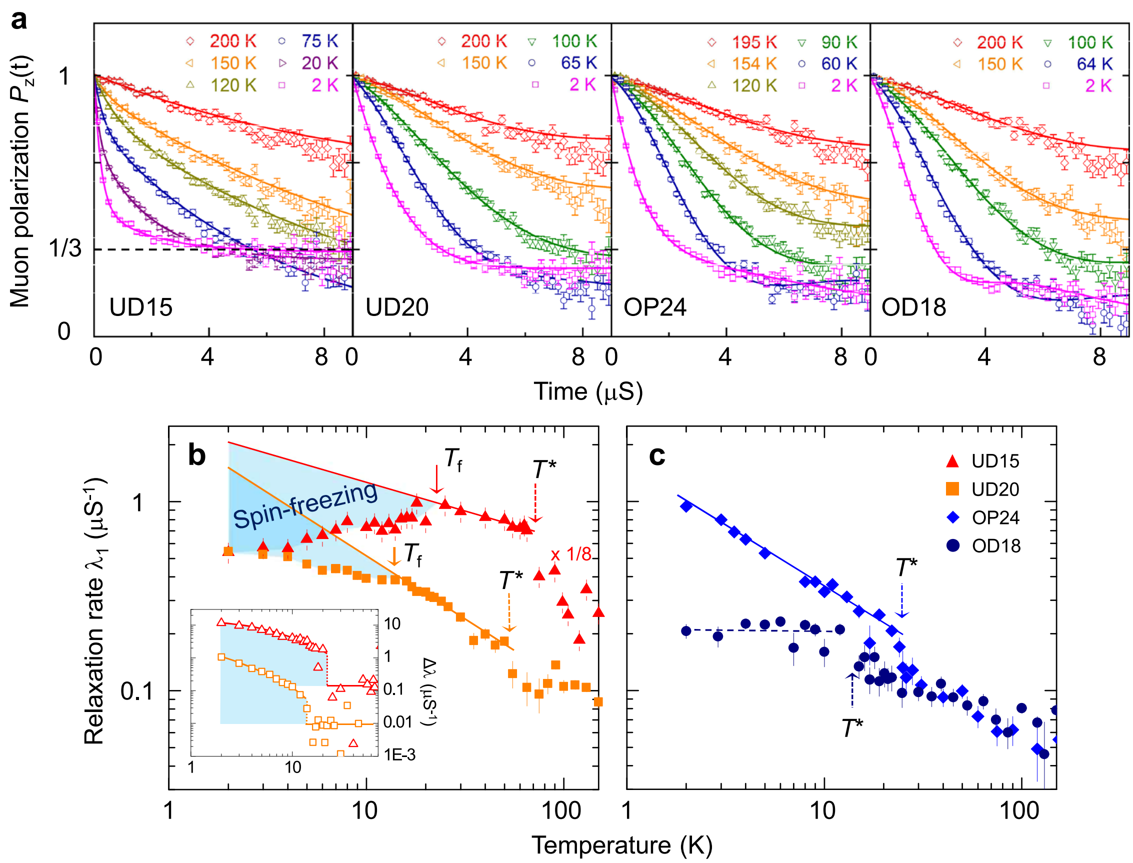

Fig. 5 | Quantum critical-like transition with dissolution of static order near OP. **a** T-dependent zero-field muon spin rotation/relaxation spectra $P_z(t)$ for samples UD15, UD20, OP24, and OD18. Solid lines show the fit to the data described in the "Methods". Error bars are statistical errors. **b**, **c** T-dependent relaxation rates $\lambda_1(T)$ for UD15, UD20, OP24, and OD18. Solid and dashed arrows indicate the transition temperatures for the spin-freezing phase T_f and fluctuating short-range-order phase T^*. The solid lines are power-law fits, $\lambda_p(T) \sim T^{-\alpha}$ (see α in Supplementary Fig. 9). The difference between the power-law fit and data, $\Delta\lambda(T) = \lambda_p(T) - \lambda_1(T)$, in the low-$T$ range denotes the fraction of frozen spins in the inset of **b**. The muon spin relaxation rate λ_1 for UD15 is scaled by a factor of 1/8 for clarity. Error bars reflect the fitting error of the $P_z(t)$ shown in (**a**).

Hole pocket with antiferromagnetic quantum phase fluctuations

We now turn to the magnetic correlations of PLCCO, measured by zero-field μSR spectroscopy. Figure 5a presents the time-differential μSR spectra of the SC compounds at selected dopings and temperatures. For all samples, the muon spin polarization $P_z(t)$ shows faster relaxation (drop) as the temperature T decreases, indicating an increase in the local magnetic fields. The lack of an oscillatory signal down to the base $T = 2$ K implies the absence of LR order in the SC phase[28] (See Supplementary Note 4). For UD sample UD15, $P_z(t)$ relaxes to 1/3 of its initial value below 20 K, suggesting the formation of SR clustered static order, i.e., a "spin-freezing phase[28]. Notably, with the higher dopings, the low-T $P_z(t)$ relaxes to values smaller than 1/3 of the initial asymmetry, while retaining its relatively fast relaxation. This implies that with increasing doping, the SR static order evolves to more dynamically fluctuating Cu spins[28].

In addition to the qualitative understanding of the muon spin relaxation, quantitative analysis of the relaxation rate λ shines more light on the quantum phase transition across the optimal doping. From the zero-field μSR spectra $P_z(t)$'s, we extracted the transverse and longitudinal components of the muon spin relaxation rate, referred to λ_1 and λ_2, respectively (see Supplementary Note 4). Specifically, we focus on doping and T-dependent λ_1, since it clearly shows the magnetic phase transition feature. Figure 5b, c display the $\lambda_1(T)$ with various doping concentrations. For UD samples UD15 and UD20, two characteristic temperatures, T^* and T_f, are identified as pointed by solid and dashed arrows, respectively. Between T^* and T_f, $\lambda_1(T)$ follows power-law dependence, $\lambda_p(T) \sim T^{-\alpha}$ (solid lines in Fig. 5b with the exponent α in Supplementary Fig. 8e), reflecting a critical slowing of the Cu spin fluctuations with decreasing T. Below T_f, the deviation of $\lambda_1(T)$ from the extrapolated $\lambda_p(T)$, as shown in Fig. 5b, demonstrates the build-up of the spin-freezing phase[29–33]. As evident from the inset of Fig. 5b, the frozen spin contribution, $\Delta\lambda(T) = \lambda_p(T) - \lambda_1(T)$, exhibits an order parameter-like increase with decreasing T. In comparison, for OD18, the absence of T_f leads to a levelling-off of $\lambda_1(T)$ below T^*, indicating the dominance of truly dynamic AF fluctuations with overdoping (Fig. 5c)[30]. More significantly, $\lambda_1(T)$ of OP24 shows a single power-law behavior below T^* (see the solid line in Fig. 5c), which means that quantum critical-like AF fluctuations dominate down to the low-T limit at optimal doping. Given that the single power law is a signature of critical behavior near a ferromagnetic or AF QCP[34–36], the doping dependence of $\lambda_1(T)$ indicates that the optimal doping of PLCCO occurs near a putative AF QCP between the SR static order and dynamically fluctuating phases[37].

Summarizing the ARPES and μSR results in an n–T phase diagram (Fig. 6), we have firmly established the relationship between Z_{hole} and antiferromagnetism. Both the mutual exclusion of the Z_{hole}-dome and LR-AF phase (See Supplementary Note 4) and the inverse proportion between the T_f and Z_{hole} signal competition between the h-pocket and static AF order. Recall that a similar anti-correlation between the nodal quasiparticle weight and AF order was suggested in t-t'-J model calculations[38]. The LR-AF phase boundary around $n \sim 0.07$ also explains why experimentally obtained Z_{hole_fit} emerges at larger doping than Z_{theory} (Fig. 4c) because the simulation excluded the LR interactions.

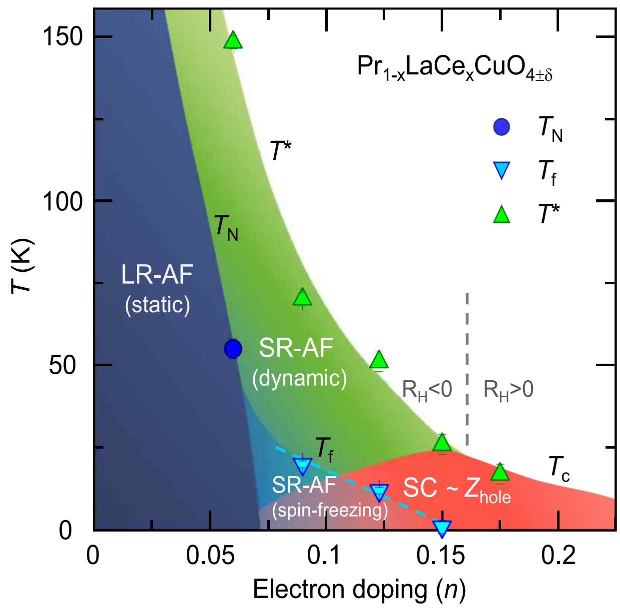

Fig. 6 | Electronic, magnetic, and SC phase diagram of PLCCO. T_N, T_f, and T^* indicate Neel, partial spin-freezing, and fluctuating short-range antiferromagnetic (SR-AF) phase transition temperatures, respectively. LR-AF represents the long-range antiferromagnetic order phase. The schematic plot of SC and Z_{hole} dome is based on the data shown in Fig. 3. The sign change in the Hall coefficient (R_H) at low-T with overdoping is shown in Supplementary Fig. 10. Error bars are attributed to the ambiguity in determining the transition temperatures from $\lambda_i(T)$ ($i = 1, 2$) (see Fig. 5 and Supplementary Fig. 9).

Conversely, the dynamic SR-AF phase seems conducive to the formation of the *h*-pocket, which is supported by the proportionality of T^* and Z_{hole} in the over-doped regime where static order is lacking. Consequently, the Z_{hole} dome, corresponding to the SC dome, is centered around the putative AF QCP, where the ground state of the SR-AF phase changes from the spin-freezing to the dynamic state. Note that near this putative QCP, we also observed a sign inversion of the Hall coefficient R_H, which has been proposed as evidence for the QCP in the electron-doped cuprates[39–41] (dashed vertical line in Fig. 6 and Supplementary Fig. 10).

Discussion

The present phase diagram established by our comprehensive ARPES and μSR experiments demonstrates that the *h*-pocket with the incipient band stems from the inhomogeneous magnetic ground state with persistent SR-AF fluctuations near the putative QCP. Specifically, regarding Z_{hole} as a measure of zero-energy DOS of the hole band at the folding center ($\pm\pi/2, \pm\pi/2$) where $|\nabla \mathbf{k}\ (\omega)|$ vanishes, the marked enhancement of Z_{hole} resembles the impact of a van Hove singularity (vHS) [42–45], namely a band-edge vHS, on the emergence of Fermi surface instability. From this perspective, the putative QCP can be interpreted as the vHS in the vicinity of E_F, enhancing the electronic susceptibility around $2\mathbf{k}_F = \mathbf{Q}(\pi, \pi)$ (Fig. 1c) and triggering the instability in spin susceptibility ascribed to quantum critical fluctuations[42–44]. Indeed, Z_{hole} is maximized as Δ_{hole} approaches 13 meV, which is in good agreement with the spin resonance energy of PLCCO[46] (Fig. 3d, e). Furthermore, vHS has generally been considered a key to strengthening superconductivity, not only in hole-doped cuprates[42–44] but also in other novel superconductors, including recently discovered twisted bilayer graphene[47]. Therefore, these observations suggest that in the electron-doped cuprates, AF instability and superconductivity are intertwined through the hole band-edge vHS.

A remaining important question is why superconductivity is predominantly dictated by the formation of small *h*-pockets instead of relatively large *e*-pockets? It has been thought that doped holes in cuprates enter the Cu 3*d*-O 2*p*-hybridized state and cause spin frustrations, while doped electrons reside in the Cu 3*d* state and cancel the spins[6]. If the holes created by the formation of *h*-pocket play the same role as the nominally doped holes, our results signal the importance of the oxygen state or the spin frustrations for the superconductivity[48]. On the other hand, referring to a previous study combining ARPES with *t*-*t*′-*t*″-*J* model calculations for $Nd_{2-x}Ce_xCuO_{4\pm\delta}$[49], electrons in the *e*-pocket may be favorably coupled to the static AF order, which competes with superconductivity. Note that the *h*-pocket in five-layered hole-doped $Ba_2Ca_4Cu_5O_{10}(F, O)_2$ previously observed by ARPES similarly implies that superconductivity can be induced by the *h*-pocket alone, without a contribution from the anti-nodal region[50]. Further systematic investigations of the orbital character of the *h*-pocket may provide clues regarding the origin of hole superconductivity in the electron-doped cuprates.

Methods

Materials

Single crystals of PLCCO with $x = 0.10$, 0.15, and 0.18 were grown by the traveling-solvent floating-zone method. All of the crystal rods were cut into small pieces along the CuO_2 plane, and annealed in a high-purity N_2 gas atmosphere at 920–930 °C and vacuum with ~10^{-5} Torr at 790 °C for 10–24 h. Subsequent air annealing was performed on some of the samples, at a temperature between 500 and 800 °C for 5–10 h. We characterized the T_c of each sample within 10% of the SC shielding volume fraction by measuring the magnetic susceptibility with a magnetic property measurement system (MPMS; Quantum Design, San Diego, CA, USA). (see Supplementary Fig. 11) Hall resistivity was measured with a physical property measurement system (PPMS; Quantum Design).

ARPES measurements

ARPES experiments were performed at beamlines 5-2 and 5-4 of the Stanford Synchrotron Radiation Lightsource (SSRL, Menlo Park, CA, USA) and TPS 39 A Nano-ARPES beamline of the National Synchrotron Radiation Research Center (NSRRC, Hsinchu City, Taiwan). Samples were cleaved in situ, and experiments were performed at temperatures below 30 K, at a pressure around 4×10^{-11} Torr. We used linearly polarized 16.5 eV photons with an overall energy resolution of ~12–15 meV for the doping dependence study described in the main text, while using 50, 55, and 85 eV photons for the complementary studies shown in the Supplementary Information (see Supplementary Note 3 and Supplementary Fig. 13). The 16.5 eV irradiation and linear polarization aligned with the *c*-axis component of the sample are suitable for the present study, as this combination tends to brighten the nodal band spectrum and enhance hot-spot features[18].

μSR measurements

The μSR measurements were performed using the M20 beamline at the TRIUMF facility (Vancouver, British Columbia, Canada). A dozen pieces of sliced PLCCO crystal (typical area: 1 cm^2) were wrapped with silver foil and attached to the sample holder. Zero-field μSR (ZF-μSR) measurements were carried out over the temperature range of 2–200 K. The physical quantity measured was the evolution of the muon depolarization $P_z(t) = [N_B(t) - \alpha N_F(t)] = [N_B(t) + \alpha N_F(t)]$, where $N_F(t)$ and $N_B(t)$ are the number of positrons counted at detectors antiparallel and parallel to the incident muon spin direction, respectively. α is the efficiency ratio between the forward and backward detectors. $P_z(t)$ conveys information about the local magnetic field distribution at the muon-stopping sites. All of the data were analyzed using the free musrfit software package[51]. All the μSR spectra in Fig. 5a were obtained by subtracting the temperature-independent constant background from the raw data and then normalizing it with the theoretical initial asymmetry $P_z(t = 0)$ estimated by the fittings. Details of the analysis process are described in Supplementary Information (see Supplementary Note 4).

CPT spectral simulations

Cluster perturbation theory (CPT) is designed to be an efficient method to estimate the $A(\mathbf{k},\omega)$ of strongly correlated systems[26,27]. When dividing the infinite plane into clusters, the Hamiltonian could be split into $H = H_c + H_{\mathrm{int}}$, where H_c contains the (open-boundary) intra-cluster operators and H_{int} contains the operators with inter-cluster indices (hopping terms for the Hubbard model). Restricting ourselves to zero temperature, we use exact diagonalization (ED) to exactly solve the cluster Green's function $G_c(\omega)$ associated with the intra-cluster Hamiltonian H_c. Then the CPT method estimates Green's function by treating H_{int} perturbatively, giving

$$G(\mathbf{k},\omega) = \frac{G_c(\omega)}{1 - V(\mathbf{k})G_c(\omega)}$$

Here $V(\mathbf{k}) = \sum_{\mathbf{R}} H_{\mathrm{int}} e^{i\mathbf{kR}}$ is the inter-cluster interactions projected to the intra-cluster coordinates. Taking the long-wavelength limit, we obtain the spectral function

$$A(\mathbf{k},\omega)_{CPT} = -\frac{1}{\pi N} Im \sum_{\sigma} G_{a,b}(\mathbf{k},\omega) e^{i\mathbf{k}(\mathbf{r}_a - \mathbf{r}_b)}$$

with a,b are intra-cluster site indices. In this paper, we employ a 4×4 cluster as the exact spectral solver. We further use an 8×8 super-clusters to obtain finer doping intervals.

Data availability

ARPES data are processed by Igor Pro 7.08 software. All data supporting the findings of this study are provided in the article and Supplementary Information files. Source data are provided in this paper.

Code availability

The codes exploited for the numerical simulations in this study are available from the corresponding authors upon request.

References

1. Keimer, B., Kivelson, S. A., Norman, M. R., Uchida, S. & Zaanen, J. From quantum matter to high-temperature superconductivity in copper oxides. *Nature* **518**, 179–186 (2015).
2. Badoux, S. et al. Critical doping for the onset of Fermi-surface reconstruction by charge-density-wave order in the cuprate superconductor $La_{2x}Sr_xCuO_4$. *Phys. Rev. X* **6**, 021004 (2016).
3. Proust, C. & Taillefer, L. The remarkable underlying ground states of cuprate superconductors. *Annu. Rev. Condens. Matter Phys.* **10**, 409–429 (2019).
4. Tsuei, C. C. & Kirtley, J. R. Pairing symmetry in cuprate superconductors. *Rev. Mod. Phys.* **72**, 969 (2000).
5. Chubukov, A. V., Pines, D. & Schmalian, J. in *The Physics of Superconductors: Conventional and High-T_c Superconductors*. Ch. 7 (eds Bennemann, K. H. & Ketterson, J. B.) (Springer, Berlin, Heidelberg, 2003).
6. Damascelli, A., Hussain, Z. & Shen, Z. X. Angle-resolved photoemission studies of the cuprate superconductors. *Rev. Mod. Phys.* **75**, 473 (2003).
7. Armitage, N. P., Fournier, P. & Greene, R. L. Progress and perspectives on electron-doped cuprates. *Rev. Mod. Phys.* **82**, 2421 (2010).
8. Das, T., Markiewicz, R. S. & Bansil, A. Superconductivity and topological Fermi surface transitions in electron-doped cuprates near optimal doping. *J. Phys. Chem. Solids* **69**, 2963–2966 (2008).
9. Harter, J. W. et al. Nodeless superconducting phase arising from a strong (π, π) antiferromagnetic phase in the infinite-layer electron doped $Sr_{1x}La_xCuO_2$ compound. *Phys. Rev. Lett.* **109**, 267001 (2012).
10. He, J. et al. Fermi surface reconstruction in electron-doped cuprates without antiferromagnetic long-range order. *Proc. Natl Acad. Sci. USA* **116**, 3449–3453 (2019).
11. Li, Y. et al. Hole pocket–driven superconductivity and its universal features in the electron-doped cuprates. *Sci. Adv.* **5**, 7349 (2019).
12. Helm, T. et al. Correlation between Fermi surface transformations and superconductivity in the electron-doped high-T_c superconductor $Nd_{2x}Ce_xCuO_4$. *Phys. Rev. B* **92**, 094501 (2015).
13. Xu, K.-J. et al. Bogoliubov quasiparticle on the Gossamer Fermi surface in electron-doped cuprates. *Science* **385**, 796–800 (2024).
14. Razzoli, E. et al. Evolution from a Nodeless gap to $d_{x^2-y^2}$-wave in underdoped La2xSrxCuO4. *Phys. Rev. Lett.* **110**, 047004 (2013).
15. Armitage, N. P. et al. Anomalous electronic structure and pseudogap effects in $Nd_{1.85}Ce_{0.15}CuO_4$. *Phys. Rev. Lett.* **87**, 147003 (2001).
16. Matsui, H. et al. Evolution of the pseudogap across the magnet-superconductor phase boundary of $Nd_{2x}Ce_xCuO_4$. *Phys. Rev. B* **75**, 224514 (2007).
17. Park, S. R. et al. Interaction of itinerant electrons and spin fluctuations in electron-doped cuprates. *Phys. Rev. B* **87**, 174527 (2013).
18. Shen, K. M. et al. Missing quasiparticles and the chemical potential puzzle in the doping evolution of the cuprate superconductors. *Phys. Rev. Lett.* **93**, 267002 (2004).
19. Mayr, M., Alvarez, G., Moreo, A. & Dagotto, E. One-particle spectral function and local density of states in a phenomenological mixed-phase model for high-temperature superconductors. *Phys. Rev. B* **73**, 014509 (2006).
20. Sato, K. et al. Coexistence of two components in magnetic excitations of $La_{2x}Sr_xCuO_4$ (x = 0.10 and 0.16). *J. Phys. Soc. Jpn.* **89**, 114703 (2020).
21. Gauvin-Ndiaye, C., Setrakian, M. & Tremblay, A.-M. S. Resilient Fermi liquid and strength of correlations near an antiferromagnetic quantum critical point. *Phys. Rev. Lett.* **128**, 087001 (2022).
22. Scalapino, D. J., Loh, E. Jr. & Hirsch, J. E. D-wave pairing near a spin-density-wave instability. *Phys. Rev. B* **34**, 8190 (1986).
23. Jiang, S., Scalapino, D. J. & White, S. R. Ground-state phase diagram of the *t-t′-J* model. *Proc. Natl Acad. Sci. USA* **118**, e2109978118 (2021).
24. Chen, Xiao et al. Electron pairing in the presence of incipient bands in iron-based superconductors. *Phys. Rev. B* **92**, 224514 (2015).
25. Rameau, J. D., Yang, H.-B. & Johnson, P. D. Application of the Lucy–Richardson deconvolution procedure to high resolution photoemission spectra. *J. Electron Spectrosc. Relat. Phenom.* **181**, 35–43 (2010).
26. Sénéchal, D., Perez, D. & Pioro-Ladrière, M. Spectral weight of the Hubbard model through cluster perturbation theory. *Phys. Rev. Lett.* **84**, 522–525 (2000).
27. Sénéchal, D., Perez, D. & Plouffe, D. Cluster perturbation theory for Hubbard models. *Phys. Rev. B* **66**, 075129 (2002).
28. Koike, Y. & Adachi, T. μSR studies on magnetism in high-T_c cuprates. *J. Phys. Soc. Jpn* **85**, 091006 (2016).
29. Guguchia, Z. et al. Pressure tuning of structure, superconductivity, and novel magnetic order in the Ce-underdoped electron-doped cuprate T-$Pr_{1.3x}La_{0.7}Ce_xCuO_4$ (x = 0.1). *Phys. Rev. B* **96**, 094515 (2017).
30. Risdiana et al. Muon spin relaxation study of the Cu spin dynamics in electron-doped high-T_c superconductor $Pr_{0.86}LaCe_{0.14}Cu_{1y}Zn_yO_4$. *Phys. Rev. B* **82**, 014506 (2010).
31. Niedermayer, C. Common phase diagram for antiferromagnetism in $La_{2x}Sr_xCuO_4$ and $Y_{1x}Ca_xBa_2Cu_3O_6$ as seen by muon spin rotation. *Phys. Rev. Lett.* **80**, 3843 (1998).
32. Panagopoulos, C., Rainford, B. D., Cooper, J. R. & Scott, C. A. Antiferromagnetic correlations versus superfluid density in $La_{2x}Sr_xCuO_4$. *Phys. C.* **341–348**, 843–846 (2000).
33. Sanna, S., Allodi, G., Concas, G., Hillier, A. D. & Renzi, R. De. Nanoscopic coexistence of magnetism and superconductivity in $YBa_2Cu_3O_{6-x}$ detected by muon spin rotation. *Phys. Rev. Lett.* **93**, 20700 (2004).

34. Tripathi, R. et al. Quantum Griffiths phase near an antiferromagnetic quantum critical point: muon spin relaxation study of $Ce(Cu_{1x}Co_x)_2Ge_2$. *Phys. Rev. B* **99**, 224424 (2019).
35. Adroja, D. T. et al. Muon spin relaxation study of non-Fermi-liquid behavior near the ferromagnetic quantum critical point in $CePd_{0.15}Rh_{0.85}$. *Phys. Rev. B* **78**, 014412 (2008).
36. Spehling, J. et al. Magnetic order and spin dynamics in the proximity of a ferromagnetic quantum critical point: A μSR study of $YbNi_4P_2$. *Phys. Rev. B* **85**, 140406(R) (2012).
37. Wilson, S. D. et al. Evolution of low-energy spin dynamics in the electron-doped high-transition-temperature superconductor $Pr_{0.88}LaCe_{0.12}CuO_4$. *Phys. Rev. B* **74**, 144514 (2006).
38. Zemljič, M. M., Prelovšek, P. & Tohyama, T. Fermi surface and pseudogap of electron-doped cuprate superconductors: Numerical study of the *t-t'-J* model. *Phys. Rev. B* **76**, 012502 (2007).
39. Dagan, Y., Qazilbash, M. M., Hill, C. P., Kulkarni, V. N. & Greene, R. L. Evidence for a quantum phase transition in $Pr_{2x}Ce_xCuO_4$ from transport measurements. *Phys. Rev. Lett.* **92**, 167001 (2004).
40. Wang, C. H. et al. Influence of doping level on the Hall coefficient and on the thermoelectric power in $Nd_{2x}Ce_xCuO_{4+\delta}$. *Phys. Rev. B* **72**, 132506 (2005).
41. Jin, K., Zhu, B. Y., Wu, B. X., Gao, L. J. & Zhao, B. R. Low-temperature Hall effect in electron-doped superconducting $La_{2x}Ce_xCuO_4$ thin films. *Phys. Rev. B* **78**, 174521 (2008).
42. Markiewicz, R. S. A survey of the van Hove scenario for high-T_c superconductivity. *J. Phys. Chem. Solids* **58**, 1179 (1997).
43. Newns, D. M., Tsuei, C. C. & Pattnaik, P. C. Anomalous isotope effect and van Hove singularity in superconducting Cu oxides. *Phys. Rev. B* **52**, 13611 (1995).
44. He, Y. et al. Superconducting fluctuations in overdoped $Bi_2Sr_2CaCu_2O_{8+\delta}$. *Phys. Rev. X* **11**, 031068 (2020).
45. Kordyuk, A. A. Electronic band structure of optimal superconductors: From cuprates to ferropnictides and back again. *Low Temp. Phys.* **44**, 477–486 (2018).
46. Wilson, S. D. et al. Resonance in the electron-doped high-transition-temperature superconductor $Pr_{0.88}LaCe_{0.12}CuO_{4\delta}$. *Nature* **442**, 59–62 (2006).
47. Cao, Y. et al. Unconventional superconductivity in magic-angle graphene superlattices. *Nature* **556**, 43–50 (2018).
48. Hirsch, J. E. & Marsiglio, F. Understanding electron-doped cuprate superconductors as hole superconductors. *Phys. C Superconduct. Appl.* **564**, 29–37 (2019).
49. Kim, C. et al. Systematics of the photoemission spectral function of cuprates: Insulators and hole- and electron-doped superconductors. *Phys. Rev. Lett.* **80**, 4245 (1998).
50. Kunisada, S. et al. Observation of small Fermi pockets protected by clean CuO_2 sheets of a high-T_c superconductor. *Science* **369**, 833–838 (2020).
51. Suter, A. & Wojek, B. M. Musrfit. A free platform-independent framework for μSR data analysis. *Phys. Procedia* **30**, 69 (2012).

Acknowledgements

We acknowledge insightful discussions with Shin-Ichi Uchida, George Sawatzky, Yu He, Dirk Wulferding, Mikyung Kim, Yangyang Li, Seyoung Park, Junwon Rhim, Ke-Jun Xu, Garam Han, Yoonyoung Koh and Alannah Hallas; ARPES experiments were performed at Beamline 5-4 and 5-2, Stanford Synchrotron Radiation Lightsource, SLAC National Accelerator Laboratory operated by the DOE Office of BES. (Proposal No. 5161) and at the TPS 39A Nano-ARPES beamline of the National Synchrotron Radiation Research Center (NSRRC, Hsinchu City, Taiwan); μSR measurements were carried out on the M20 beamline at the TRIUMF facility (Vancouver, Canada). This project was undertaken thanks in part to funding from the Canada First Research Excellence Fund, Quantum Materials, and Future Technologies Program. C.K. acknowledges support from NRF (No. 2022R1A3B1077234 and RS-2023-00258359). H.E. acknowledges JSPS KAKENHI (Grant No. JP19H05823). The work at SKKU was supported by the National Research Foundation (NRF) of Korea (Grant Nos. RS-2023-00209121 and 2020R1A5A1016518). S.-R.P. acknowledges the National Research Foundation of Korea (NRF) (Grant No. NRF-2020R1A2C1011439). The work at IBS-CINAP was supported by the Institute for Basic Science (IBS-R011-Y3). Z.S. and Y.W. acknowledge support from the Air Force Office of Scientific Research Young Investigator Program under grant FA9550-23-1-0153. The spectral simulations used resources of the National Energy Research Scientific Computing Center (NERSC), a U.S. Department of Energy Office of Science User Facility located at Lawrence Berkeley National Laboratory, operated under Contract No. DE-AC02-05CH11231 using NERSC award BES-ERCAP0023181.

Author contributions

D.S., S.L., S.-R.P., H.E., K.-Y.C., and C.K. conceived and designed the experiments with suggestions from S.C., S.I., and Y.Y.; Z.S. and Y.W. performed theoretical calculations; D.S., W.J., and S.I. grew and characterized the PLCCO single crystals; D.S., W.J., W.K., S.J., and C.-M.C. performed the ARPES measurements; S.L., W.L., and K.-Y.C. performed the μSR measurements; D.S., W.J., S.J. and J.K. analyzed the ARPES experimental data; S.L. and W.L. analyzed the μSR experimental data; D.S., S.L., Y.W., S.C., W.K., K.-Y.C., and C.K. wrote the manuscript with input from S.-R.P., H.E., and contributions from all authors.

Competing interests

The authors declare no competing interests.

Additional information

Supplementary information The online version contains supplementary material available at https://doi.org/10.1038/s41467-025-57942-z.

Correspondence and requests for materials should be addressed to Yao Wang, Kwang-Yong Choi or C. Kim.

Peer review information *Nature Communications* thanks the anonymous reviewers for their contribution to the peer review of this work. A peer review file is available.